Materials Science & Engineering C 120 (2021) 111735

Contents lists available at ScienceDirect

Materials Science & Engineering C

journal homepage: www.elsevier.com/locate/msec

TiO_2 bioactive implant surfaces doped with specific amount of Sr modulate mineralization

A.I. Costa [a,b,*], S. Gemini-Piperni [c,d], A.C. Alves [a], N.A. Costa [d,e], N.R. Checca [f], P.E. Leite [g,h], L. A. Rocha [d,i], A.M.P. Pinto [a,j], F. Toptan [a,d], A.L. Rossi [f], A.R. Ribeiro [c,d,h,1]

[a] CMEMS-UMinho – Center of MicroElectroMechanical Systems, University of Minho, Guimarães, Portugal
[b] DEMM – Department of Metallurgical and Materials Engineering, Faculty of Engineering of the University of Porto, Porto, Portugal
[c] Postgraduate Program of Translational Biomedicine, University Grande Rio, Duque de Caxias, Brazil
[d] IBTN/Br – Brazilian Branch of the Institute of Biomaterials, Tribocorrosion and Nanomedicine, São Paulo State University, Bauru, São Paulo, Brazil
[e] Postgraduate Program in Materials Science and Technology, São Paulo State University, Bauru, São Paulo, Brazil
[f] CBPF – Brazilian Centre for Research in Physics, Rio de Janeiro, Brazil
[g] Directory of Life Sciences Applied Metrology, National Institute of Metrology Quality and Technology, Xérem, Rio de Janeiro, Brazil
[h] Postgraduate Program in Biotechnology, National Institute of Metrology Quality and Technology, Xérem, Rio de Janeiro, Brazil
[i] Faculty of Science, Department of Physics, São Paulo State University, Bauru, São Paulo, Brazil
[j] DEM – Department of Mechanical Engineering, University of Minho, Guimarães, Portugal

ARTICLE INFO

Keywords:
Sr
Micro-arc oxidation
TiO_2
Orthopedics implants

ABSTRACT

One of the main problems that remain in the implant industry is poor osseointegration due to bioinertness of implants. In order to promote bioactivity, calcium (Ca), phosphorus (P) and strontium (Sr) were incorporated into a TiO_2 porous layer produced by micro-arc oxidation. Ca and P as bioactive elements are already well reported in the literature, however, the knowledge of the effect of Sr is still limited. In the present work, the effect of various amounts of Sr was evaluated and the morphology, chemical composition and crystal structure of the oxide layer were investigated. Furthermore, *in vitro* studies were carried out using human osteoblast-like cells.

The oxide layer formed showed a triplex structure, where higher incorporation of Sr increased Ca/P ratio, amount of rutile and promoted the formation of $SrTiO_3$ compound. Biological tests revealed that lower concentrations of Sr did not compromise initial cell adhesion neither viability and interestingly improved mineralization. However, higher concentration of Sr (and consequent higher amount of rutile) showed to induce collagen secretion but with compromised mineralization, possibly due to a delayed mineralization process or induced precipitation of deficient hydroxyapatite. Ca-P-TiO_2 porous layer with less concentration of Sr seems to be an ideal candidate for bone implants.

1. Introduction

In most OECD countries, the number of hip replacements has increased by 30% between 2000 and 2015 and currently, more than 1 million total hip replacements are performed every year in the world [1,2]. The existing prostheses may be successful in restoring function, thereby increasing the quality of life of millions of people, but present some concerns in the medium/long term. Unfortunately, nowadays it was estimated that 75% of the hip implants had a lifetime of 15–20 years [3] mainly due to tendencies to fail after medium/long term use because of various reasons, such as low wear resistance, lack of bioactivity and poor osseointegration due to the bioinertness of the implant surface [4–6]. In order to solve these problems and to improve the lifetime of implants, surface modification by anodic treatment under micro-arc oxidation (MAO) regime, also called plasma electrolytic oxidation (PEO), is presented as a favourable solution. MAO has shown capabilities to improve the most important surface characteristics of implants such as improving the bioactivity by the incorporation of bioactive

* Corresponding author at: CMEMS-UMinho – Center of MicroElectroMechanical Systems, University of Minho, Department of Mechanical Engineering, Campus de Azurém, 4800-058 Guimarães, Portugal.
E-mail address: a66848@alunos.uminho.pt (A.I. Costa).
[1] The author is currently at: 3B's Research Group, Research Institute on Biomaterials, Biodegradables and Biomimetics, Headquarters of the European Institute of Excellence on Tissue Engineering and Regenerative Medicine, University of Minho, Guimarães, Portugal.

https://doi.org/10.1016/j.msec.2020.111735
Received 5 June 2020; Received in revised form 30 October 2020; Accepted 11 November 2020
Available online 14 November 2020

elements, tailoring the oxide phases, roughness, porosity and topography that also eventually defines the wettability in a way to be more suitable for cells [7–10]. MAO contributed to an improved adhesion, proliferation and differentiation of cells, blood compatibility, reduction of the haemolysis rate, extended dynamic coagulation time, reduction of the amount of platelet adhesion and degree of deformation, among other properties [7–10], like improved corrosion [11–16] and tribocorrosion [17–21] behaviour.

MAO promotes the incorporation of bioactive elements in order to give biofunction to bioinert metal implants. Regarding bioactive elements, the major chemical element found in the bone is Ca, followed by P, but there are at least a dozen of other chemical elements in its constitution. For example, most Sr (99%) present in the human body is deposited in the bone due to its superior ability to bind with hydroxyapatite (HAP) *i.e.* with the mineral phase of bone [22–29]. New compact bone contains at least three times more Sr than old compact bone, while new cancellous bone contains at least two times more Sr than old cancellous bone. This can be explained by the fact that in the newly formed bone, Sr is not only incorporated into the crystals (as heteroionic substitutions) but it is also included onto their surface (adsorption and exchange). In contrast in old bone, Sr is almost exclusively taken up onto the surface of crystals since almost no heteroionic substitution occurs afterwards [30]. Sr has an effect on osteoblast proliferation and osteoclast resorption with consequently stimulation of bone growth and inhibition of bone resorption [31,32]. Thus, Sr is accounted as a potential bioactive element showing promising results *in vitro* [31–34] and *in vivo* [25,33,35–37].

Nowadays Sr has been widely used in the biomedical field, as implants [31–34] and drug deliveries systems [34]. However, there are many concerns with its long-term effectiveness and performance because of possible Sr toxicity that has been shown to present a dose-dependent behaviour [30,38,39]. For example, some cardiovascular side effects were observed when strontium ranelate [28] was used as therapeutics to treat osteoporosis.

Sr on TiO_2 layers [35,40,41,43–45] showed promising results for biomedical applications. Lee et al. [40] studied the incorporation of Sr, Ca and P on anodized Ti and stated that the lowest Sr content provided a preferential surface for osteoblastic cell proliferation. Zhang et al. [43] showed that osteoblastic cell adhesion on Sr-incorporated TiO_2 was significantly enhanced compared with the Sr-free TiO_2. Sato et al. [44] studied the effect of the Sr addition along with Ca and P to a TiO_2 layer formed by MAO and the results showed a small inhibitory effect on preosteoblasts cell proliferation, however osteogenic differentiation and mineralization was observed. Based on our knowledge, few studies explored in in-depth the effect of Sr incorporation on Ca-P on TiO_2 layers and there is no consensus in which range of Sr is more beneficial for mineralization. There is still limited information regarding the effect of the amount of Sr on the composition, microstructure and long-term biological responses of Sr-TiO_2 surfaces.

A lot of studies that evaluated the effect of Sr in a layer with Ca are substituting Ca for Sr [31,35,44]. We combined the work of Kung et al. [24,29,46], where the authors used 0.0013 and 0.013 of strontium hydroxide to produce Ca-P-Sr TiO_2 porous surfaces, and a recent work that showed the behaviour of Sr can be promoted in a calcium rich microenvironment [47]. Xie et al. [47] hypothesize that the effect of strontium on bone regeneration is related to the concentration of calcium and concluded that Sr is more potentially effective for bone regeneration in combination with an environment having a high concentration of calcium ions. In fact, strontium inhibits bone regeneration with low dose calcium and promotes bone regeneration with a high dose of calcium *in vitro*. In addition, we also decide to work with 0.35 M of calcium acetate, since previous works showed that higher Ca concentration in the MAO electrolyte solution had a positive effect on the surface properties, chemical composition, cell evaluation and tribocorrosion behaviour [7,9,19,17,49]. In the end, we continued the studies with 0.35 M of calcium acetate and combined with the addition of 3 concentrations of strontium hydroxide (0.0013, 0.013 and 0.13 M).

Hence, in the present work, the effect of the incorporation of several concentrations of Sr on Ca-P-TiO_2 layers was evaluated and discussed. A detailed characterization of Sr-MAO oxide layer was performed with high-resolution techniques since there is a lack of information regarding their structure. Osteoblasts/Ca-P-Sr TiO_2 layers interface, cell adhesion, viability and mineralization were evaluated.

2. Materials and methods

2.1. Samples preparation and characterization

Prior to MAO treatment, Ti plates (1 × 1 cm) were ground with 320# *SiC* papers and then etched in a Kroll's reagent solution (1:1:1 for HF: HNO_3:H_2O) for 10 s. Then the samples were ultrasonically cleaned in propanol for 15 min followed by 10 min in distilled water and dried with warm air.

After surface pre-treatment, anodic treatment was carried out under MAO regime using 200 mL of a mixture of 0.02 M of β-glycerophosphate disodium salt pentahydrate (β-GP, Alfa Aesar), 0.35 M of calcium acetate monohydrate (CA, Alfa Aesar) electrolyte and 0.0013 M, 0.013 M or 0.13 M of strontium hydroxide octahydrate (SH, Alfa Aesar). The electrolyte was chosen in order to incorporate bio-active species, namely P (from β-GP), Ca (from CA) and Sr (from SH). Electrical conductivity was measured (WTW Inolab conductivity meter Level 1) for the 4 conditions of electrolyte under study, at 22 ± 1 °C, with at least 5 measures per condition. Depending on the concentration of SH on the electrolyte, the groups of samples were named CaP (no SH added), mSr (0.0013 M of SH), mmSr (0.013 M of SH) and mmmSr (0.0013 M of SH). Table 1 gives the details of the MAO process, presenting the electrolyte composition with the respective group code and electrolyte conductivity (ms/cm). MAO treatment was performed at room temperature under a constant voltage of 300 V with a limiting current of 2.60 A during 1 min (*i.e.* wait to reach 300 V and then count 1 min) using a direct current (DC) power supply. The samples were connected as anode and a platinum sheet was used as cathode. The anode area was 2.8 cm^2 and the cathode area was 13 cm^2. The distance between the cathode and the anode was 8 cm and all the MAO treatments were carried out under turbulent regime at 200 rpm. After MAO treatment, the samples were cleaned with distilled water and air-dried. Each electrolyte was reused to produce a maximum of 5 samples after preliminary analyses ensuring the reproducibility in terms of morphology, oxide phases and chemical structure.

The topography, microstructure and chemical composition of the oxide layers formed on the surface were analysed by FEI Nova 200 field emission gun scanning electron microscope (FEG-SEM) equipped with energy dispersive X-ray spectroscopy (EDS). The distributions of pore size of the MAO layers were calculated using a point-counting method adapted from ASTM E562, where a grid (17 lines parallel to each other with a constant spacing of 0.03 mm) was superimposed on the micrographs. All the pores intersecting the lines had their diameters measured. Three SEM images were taken for each sample in at least 3 different zones of the surface and 3 samples were used per group. EDS mapping was performed using a silicon drift detector (SDD) (Oxford),

Table 1
Electrolyte composition with respective group nomenclature and electrolyte conductivity (ms/cm).

Electrolyte composition	Group nomenclature	Electrolyte conductivity (ms/cm)
0,35 M CA + 0,02 B-GP	CaP	21.5 ± 0.3
0,35 CA + 0,02 B-GP + 0,0013 M SrH	mSr	21.9 ± 0.1
0,35 CA + 0,02 B-GP + 0,013 M SrH	mmSr	22.6 ± 0.1
0,35 CA + 0,02 B-GP + 0,13 M SrH	mmmSr	33.6 ± 0.1

equipped to scanning electron microscope, using AZtec (Oxford) software.

Crystalline structure was characterized by XRD (Cu Kα radiation, Bruker D8 Discover) with a scanning range (2Θ) of 20° to 100° at glancing incidence angle. At least three samples were evaluated per group in order to assure the reproducibility. Phase identification was performed with the help of the standard JCPDS database (JCPDS database: 00-044-1294 for Ti, 01-089-4203 for TiO_2 – anatase and 01-078-1508 for TiO_2 – rutile) and the phase percentage of the oxide layer obtained by MAO was calculated following Eq. (1):

$$\%phase_{\alpha} = \frac{\sum I_{apeaks}}{\sum I_{allpeaks}} \quad (1)$$

The elemental composition and chemical bonding of the top of the surface of the oxide layers were evaluated by X-ray photoelectron spectroscopy (XPS) using a SPECS PHOIBOS 100/150 spectrometer with a 150 mm hemispherical analyser operating with X-ray energy source of 1486.6 eV from a polychromatic Al (Kα) radiation in 30° as take-off angle, E_{pass} of 30.0 eV, using an energy step of 0.5 eV (for the survey spectrum) and 0.02 eV (for the high-resolution spectra over each element peak). The energy band peak deconvolution was made using the CASA-XPS software and the NIST-XPS database for the envelope peaks C 1s, O 1s, Ti 2p, Ca 2p, P 2p and Sr 3d binding energies. C 1s (284.6 eV) was used as calibration energy.

2.2. Surface preparation and cell culture

Prior to cell culture experiments, Ti plates bio-functionalized (including their backsides) were sterilized in a sterile culture hood by 2 hour immersion in ethanol 70% (V/V) followed by 2 h of UV light irradiation.

Human osteoblast-like MG-63 cells (ATCC number: CRL-1427™) were provided by Rio de Janeiro cell bank and were used for evaluation of cell-surface interactions. MG-63 osteoblastic cells were cultured at 37 °C and 5% CO_2 in a cell growth medium consisting of Dulbecco's modified Eagle's medium (DMEM, Gibco) supplemented with 10% (V/V) fetal bovine serum (FBS, Gibco) and 1% (V/V) of an antibiotic (100 U mL^{-1} of penicillin-streptomycin, BioReagent). Cell culture experiments were performed at approximately 80% confluence.

2.3. Cell adhesion

For adhesion experiments, MG-63 cells were seeded with a density of 1×10^4 cells per cm^2 on the surfaces placed in a 24-well plate and grown at 37 °C in fully humidified atmosphere containing 5% CO_2 alternatively for 4 and 24 h. Evaluation of the cell adhesion experiments was performed by fluorescent staining of the actin cytoskeleton (using Alexa Fluor 546 Phalloidin, Thermo Fisher Scientific, A22283) and the nucleus (4′,6-diamidino-2-phenylindole-dihydrochloride, DAPI, Sigma-Aldrich, F6057). Cells adherent to the disks after 4 and 24 h were fixed with 4% paraformaldehyde (PFA), permeabilized with 0.1% (v/v) Triton X-100, and the unspecific staining was blocked by incubation in 3% BSA before exposure to Alexa Fluor 546 Phalloidin and DAPI. Samples were examined with a fluorescence microscope inverted with a digital camera Axio Observer A1 (Zeiss) equipped with AxioCAM MRm. For each testing condition and time point of experiment, at least four samples were used and two independent experiments were carried out.

2.4. Cell viability

For viability experiments, MG-63 cells were seeded (cell density of 2×10^4 cells per cm^2) on the surfaces placed in a 24-well plate. All the cell-containing samples were incubated at 37 °C in a fully humidified atmosphere containing 5% CO_2 for 24 h. Then LIVE/DEAD® assay was performed to access the cytotoxicity of the surfaces and was used in accordance with the manufacturer's instructions (LIVE/DEAD® Viability/cytotoxicity kit, Thermo Fisher Scientific, L3224). The kit contained two probes: calcein acetoxymethyl and ethidium homodimer. Active intracellular esterase of living cells converts calcein acetoxymethyl to calcein to generate green fluorescence. On the other hand, ethidium homodimer binds the nucleic acids but it is not permeable to cell membrane. In this way, it can only enter on the dead cells with a broken cell membrane producing red nuclear fluorescence. Finally, the total number of live and dead cells adhered on materials surfaces was determined by fluorescence microscope inverted with digital camera Axio Observer A1 (Zeiss) equipped with digital camera AxioCAM MRm (Zeiss). A total number of 12 images were acquired for each group, from which the number of live (green) and dead (red) cells were counted. For each testing condition, at least three samples were used and two independent experiments were carried out.

2.5. Cell mineralization

For the 21 days cell culture experiments, in order to evaluate osteoblastic mineralization, MG-63 was seeded with a density of 1×10^5 cells per cm^2 in incomplete osteogenic medium. The medium component are Dulbecco's modified Eagle's medium (DMEM, Gibco) high glucose, supplemented with 10% (V/V) fetal bovine serum (FBS, Gibco) and 1% (V/V) of an antibiotic (100 U mL^{-1} of penicillin-streptomycin, BioReagent), and 0,01 M β-glycerophosphate (Sigma-Aldrich) and 50 μg mL^{-1} of L-ascorbic acid (Sigma-Aldrich) to induce cell mineralization. The culture medium was replenished every 7 days. After 21 days, alizarin red-s staining (ARS) of MG-63 osteoblasts was conducted to detect the ability to form calcified deposits. All specimens were stained with 1% alizarin red-s (Sigma-Aldrich, A5533-25G) solution at room temperature and then rinsed with ultra-pure water. Alizarin red-s was dissolved using a solution of 0.5 N HCl with 5% SDS and the absorbance value of each well was quantified spectrophotometrically using a microplate reader (Biotek synergy 2 multi-mode detection with gen5 software) at a wavelength of 450 nm. Results were reported as optical density (OD) values. For each testing condition, at least four samples were used and two independent experiments were carried out.

Evaluation of the cell organic matrix was performed. Cells were fixed in PFA 4%, permeabilized with 0.1% (v/v) Triton X-100, and the unspecific staining was blocked by incubation in 1% BSA. Following triple staining for the actin cytoskeleton (using Alexa Fluor 546 Phalloidin, Thermo Fisher Scientific, A22283), for the level of collagen type I (Monoclonal Anti-Collagen Type I, Sigma-Aldrich, C2456-2Ml) and for the nucleus (4′,6-diamidino-2-phenylindole-dihydrochloride, DAPI, Sigma-Aldrich, F6057) was performed. Samples were then examined with a fluorescence microscope inverted with a digital camera Axio Observer A1 (Zeiss) equipped with AxioCAM MRm. For each testing condition, at least three samples were used and two independent experiments were carried out.

2.6. Cell morphology

In order to investigate cell morphology at different culture time points (4, 24 h and 21 days), cells adhered to the surface were fixed with Karnovsky, post-fixed with 1% Osmium tetroxide (OsO_4, Alpha Aesar), 0,8% potassium ferrocyanidethen dehydrated through a graded series of alcohol (50%, 60%, 70%, 80%, 90%, 95% and 100%), then dried using hexamethyldisilazane (HDMS, Sigma-Aldrich). Afterward, specimens were sputter-coated with gold and cell morphology was observed by SEM (FEG-SEM Tescan-Lyra 3 microscope).

An Auriga 40 Dual Beam instrument equipped with a Focused Ion Beam (FIB) using a gallium ion source and a SEM was used in order to analyse the interface between osteoblast and oxide layer. The samples were fixed and dehydrated as previously described. Cross-sections were performed on osteoblast adhered for 24. Slices and millings were performed using ion currents between 1 and 5 nA and beam energy of 30

keV. Lower ion beam currents (~200 pA) were used to polish and clean the cross-section surface. Images were recorded using the electron beam accelerated with 5 kV and a backscattered detector.

2.7. Cytokines expression

MG-63 cells were cultivated during 21 days on MAO-treated surfaces and 100 μL of the supernatants were collected for cytokine analysis for all the conditions. The supernatant was kept frozen at −80 °C. Analysis was performed following the manufactures' recommendations for the MAGPIX reagent kit for identification of cytokines (cytokines-plex panel, Biorad). IL-1β, IL-1ra, IL-2, IL-4, IL-5, IL-6, IL-7, IL-8, IL-9, IL-10, IL-12p70, IL-13, IL-15, IL-17A, IP-10, IFN-γ, TNFα, VEGF, bFGF, MIP-1α, MIP-1β, MCP-1, PDGF-BB, RANTES, GM-CSF, G-CSF, Eotaxin were included in the analysis. Each step was preceded by washing using an automated washing station (BioPlex-MAGPIX, Biorad).

2.8. Statistical analysis

Statistical analysis was performed using one-way analysis of the variance (ANOVA) followed by Tuckey test in order to access the differences in the variance between the groups in the biological assays, using a significance level of $p < 0.05$.

3. Results and discussion

3.1. Surface characterization

Fig. 1 shows the top surface of the MAO samples with a morphology that did not change through the studied conditions: a typical rough micro-porous network with volcano-like shape (also named as crater-like structure) resultant from the micro-discharges channels that occur during the MAO treatment [50]. It was observed that most of the holes were well separated and homogeneously distributed over the surface for all conditions. In this way, the incorporation of Sr was not influencing the morphology of the surface, neither the pore size distribution nor the average pore size (Fig. 1). Sato et al. [44] also reported no significant effect of Sr concentrations in the morphology of MAO layers. The oxide layer presented a distribution of the pore size between 0.5 and 5 μm with an average size around 2 μm.

Supplementary video obtained by slice-and-view in a dual beam microscope shows a detailed look of the cross-section at the oxide layer produced by MAO treatment. Porosity along the cross-section showed interconnectivity between the pores along the oxide with some closed pores. Thickness of MAO layers was accessed by FIB cross-section cuts for all the groups under study and the mean value for thickness obtained was 4.7 ± 0.9 μm. The oxide layer presented the typical triplex structure composed by a compact and thin layer next to the bulk material, called barrier film, then an inner porous layer having small pores and an outer porous layer having bigger pores. A similar detailed cross-section was already presented by Alves et al. [49] and the authors stated that the barrier film was responsible for good corrosion protection. In this way, MAO treatments allow the formation of rough, porous titanium oxide layer with a wide range of pore size and distribution in the micro- and nano-scale, excellent conditions that influence bone cell behaviour [51].

During MAO treatments, high temperatures were reached promoting the localized melting of the oxide. In this way, bioactive elements present on the electrolyte were incorporated in the oxide layer during its formation [11]. Elements like Ti, O, Ca, P and especially Sr were detected in the elemental analysis by EDS, showing that the incorporation of Sr in the MAO layer was successful for the three conditions (Fig. 2a). EDS confirmed the incorporation of Sr having an at.% content of 0.32 ± 0.03, 0.57 ± 0.04 and 2.66 ± 0.09 on mSr, mmSr and mmmSr groups, respectively. On the group with higher amount of Sr, Ca and P were incorporated less than in the other conditions, since Sr was highly available in the electrolyte. Despite that, Ca/P ratio obtained was above the one found in HAP (1.67) in all the conditions. Superior Ca/P ratio can be favourable since Ca presents a faster dissolution than P in physiologic solution, even though that dissolution is what promotes the formation of HAP [52–54]. Sr was distributed uniformly on the surface for all the conditions, as it can be observed in Fig. 2a. According with Lu et al. [55], it is easier to incorporate Ca and Sr than P. The cationic elements as Ca^{2+} and Sr^{2+} in the electrolyte were more attracted to the cathode and repulsed from the anode during the MAO treatment because of the strong electric field. In fact, calcium acetate and strontium hydroxide were easily dissolved in the water and in this way, they combined with OH^- ions and moved towards the sparking areas incorporated in the oxide layer while the voltage increased.

X-ray diffraction patterns for all conditions are shown in Fig. 2b. The major characteristic peaks presented corresponded to Ti and TiO_2 in the form of anatase and rutile. A large number of plasma discharges provided enough energy to reach temperatures to allow the formation of both metastable anatase and stable rutile [56]. The percentage of rutile phases were calculated by Eq. (1) and the results obtained were 42 ± 3 for CaP, 40 ± 3 for mSr, 39 ± 3 for mmSr, and 48 ± 2 for mmmSr. These results suggest that the condition with the highest level of Sr (mmmSr),

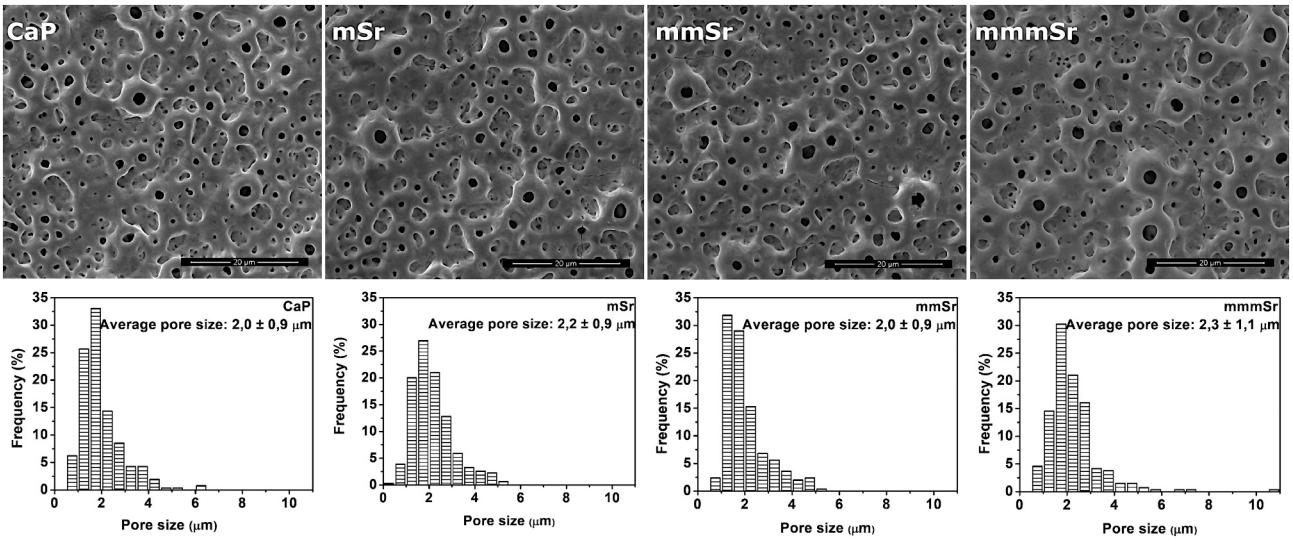

Fig. 1. Representative SE-SEM images together with corresponding pore size distribution and average pore size for all conditions.

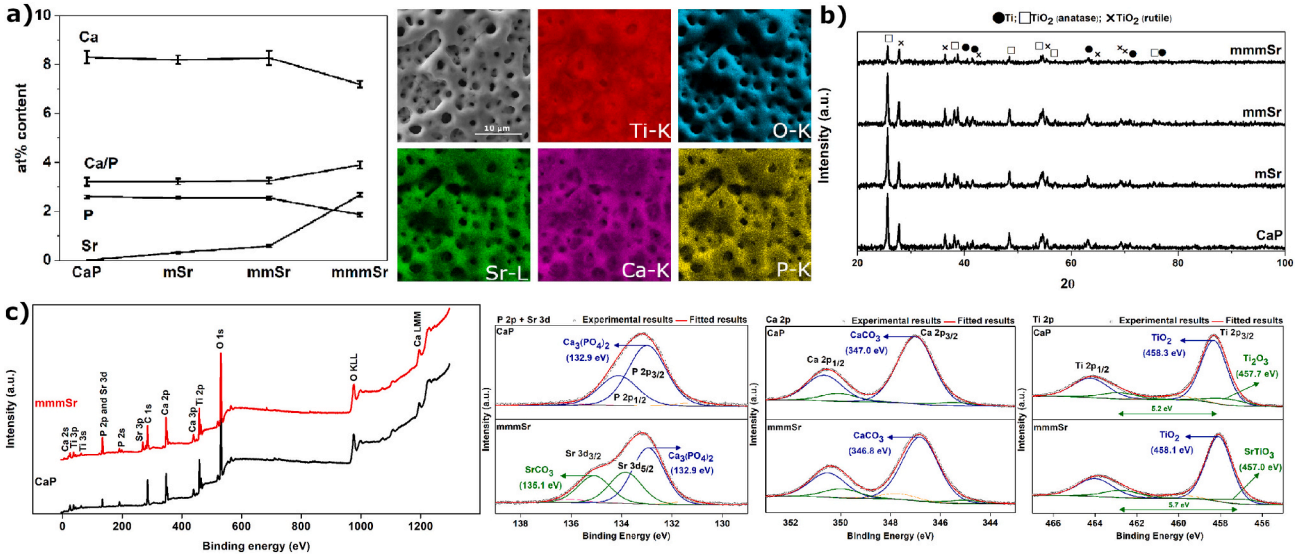

Fig. 2. Surface characterization: a) elemental concentrations (at.%) by EDS analysis for all conditions and SE-SEM and EDS mapping images (without overlay) for mmmSr group; b) crystal structure obtained by XRD analysis for all conditions; c) XPS spectra with the respective high-resolution spectrum and respective deconvolution for P 2p and Sr 3d, Ca 2p and Ti 2p for CaP and mmmSr groups.

led to an increase in the rutile phase. In fact, as it was shown in Table 1, the addition of Sr after a certain amount changed the conductivity of the electrolyte. It is known that the conductivity of the electrolyte influences the dielectric breakdown potential which may lead to differences in the oxide phases formed during MAO treatment. Hence, on mmmSr condition, the dielectric breakdown potential was probably reached sooner leading to higher temperatures for a longer period, facilitating the formation of more amount of rutile [56]. From literature, it is known that rutile is formed at higher temperatures and at higher voltages when compared with anatase [57,58]. Teng et al. [93] also reported the same trend in the MAO treatment where the relative intensity of the rutile peak increased with a higher amount of Sr. However, this phenomenon is dependent on the technique that is used to incorporate Sr. For instance, Xu et al. [38] incorporated Sr in TiO_2 by plasma spraying and stated that with the increased Sr amount in the coating, the relative amount of anatase increased, showing that Sr incorporation can suppress the anatase to rutile transformation.

The distribution of the oxide phases within the Sr-MAO-treated Ti oxide layers is not yet clarified. Previously, Ribeiro et al. [9] and Oliveira et al. [19] that produced MAO layers on Ti with similar processing parameters, including the Ca/P ratio stated that the oxide layer was a mixture of anatase and rutile phases where rutile was preferentially located on the top of the volcanoes structures, while the valleys of the oxide were mainly composed of anatase. In addition, wear and tribo-corrosion resistance was also improved by the presence of rutile phases on the oxide layer [9,14,17–19].

XPS analysis was used to investigate the surface chemistry of the oxide layers formed by MAO in order to assess the effect of the Sr incorporation. The survey spectra of the CaP specimen, presented in Fig. 2c, revealed peaks associated with Ca 2s, Ti 3p, Ti 3s, P 2p, Sr 3d, P 2s, Sr 3p, C 1s, Ca 3p, Ti 2p, O 1s, O KLL, Ca LMM. The addition of Sr resulted in a survey with peaks associated with the presence of Sr 3d and Sr 3p, confirming the incorporation of Sr into the oxide layer, as in accordance with the EDS analysis presented in Fig. 2a. Fig. 2c also shows the high-resolution spectra for P 2p and Sr 3d, Ti 2p and Ca 2p, regions, respectively, for CaP and mmmSr groups. P 2p envelope was fitted with two peaks. As presented, the binding energy found at 132.9 eV into the P 2p envelope reinforces that PO_4^{3-} groups were present on the surface of the different films [36,59–62]. On the mmmSr spectra, P 2p and Sr 3d peaks overlapped around 134/135 eV, and the Sr $3d_{5/2}$ component detected at 133.8 eV might be assigned to strontium carbonate ($SrCO_3$) species, due to further oxidation of the metallic strontium with exposure to air [25,63]. In Fig. 2c, high-energy resolution analysis of individual peaks for Ca 2p are presented, where the significant contributions at 347.0 and 346.8 eV for CaP and mmmSr groups could be attributed to the presence of $CaCO_3$ compounds, as well as Ca-O compounds [36,59–61,64]. It is also suggested that the minor Ca $2p_{3/2}$ contributions at 345.5 and 345.0 eV for CaP and mmmSr groups, respectively, corresponded to metallic Ca species [59,65]. As depicted in Fig. 2c, four major peaks were fitted for each condition in the Ti 2p region, decomposing into two doublets, where the major one (represented by the Ti $2p_{3/2}$ peaks at 458.3 and 458.1 eV for CaP and mmmSr groups, respectively) corresponded to TiO_2 [59,60,66]. For CaP group, the Ti $2p_{3/2}$ peak found at 457.7 eV with a doublet separation of 5.2 eV may be associated with the Ti^{3+} valence state from Ti_2O_3 [59,60,66]. On the other hand, for the mmmSr group, the additional doublet with spin-orbit splitting of 5.7 eV could be related to the $SrTiO_3$ compound, which is identified by Ti $2p_{3/2}$ peak at 457.0 eV.

3.2. Biological assays

The behaviour of MG-63 osteoblast cells was evaluated in terms of cell adhesion, viability, and mineralization. It is known from the literature that biological results are due to the combination of several physicochemical characteristics of the surfaces, hence, we suppose that the biological results are the combined action of Sr within the coating as well as the Sr leached, together with oxide morphology, chemical composition and crystal structure. Fig. 3a presents the initial cell adhesion area (4 h after seeding) where no significant differences between all the conditions was observed. However, after 24 h, a statistically significant difference in the cell adhesion area was observed between mSr and mmmSr. Fig. 3b shows the fluorescence microscope images after 24 h of cell adhesion, where it was possible to see a significant enhancement of cell adhesion and spreading only for CaP and mSr groups. Cells presented an organized actin cytoskeleton with a spindle morphology. Hence, these results showed that higher amount of Sr (mmmSr) may have a detrimental effect on cell adhesion after 24 h (Fig. 3a). This poor cell adhesion may be due to the combined action of chemical composition (higher quantity of Sr) and different quantities of crystal structures (higher amount of rutile in mmmSr) on the oxide layer. He et al. [67] showed that the crystal structure influence osteoblastic cells grown, with osteoblasts presenting the largest spreading on the

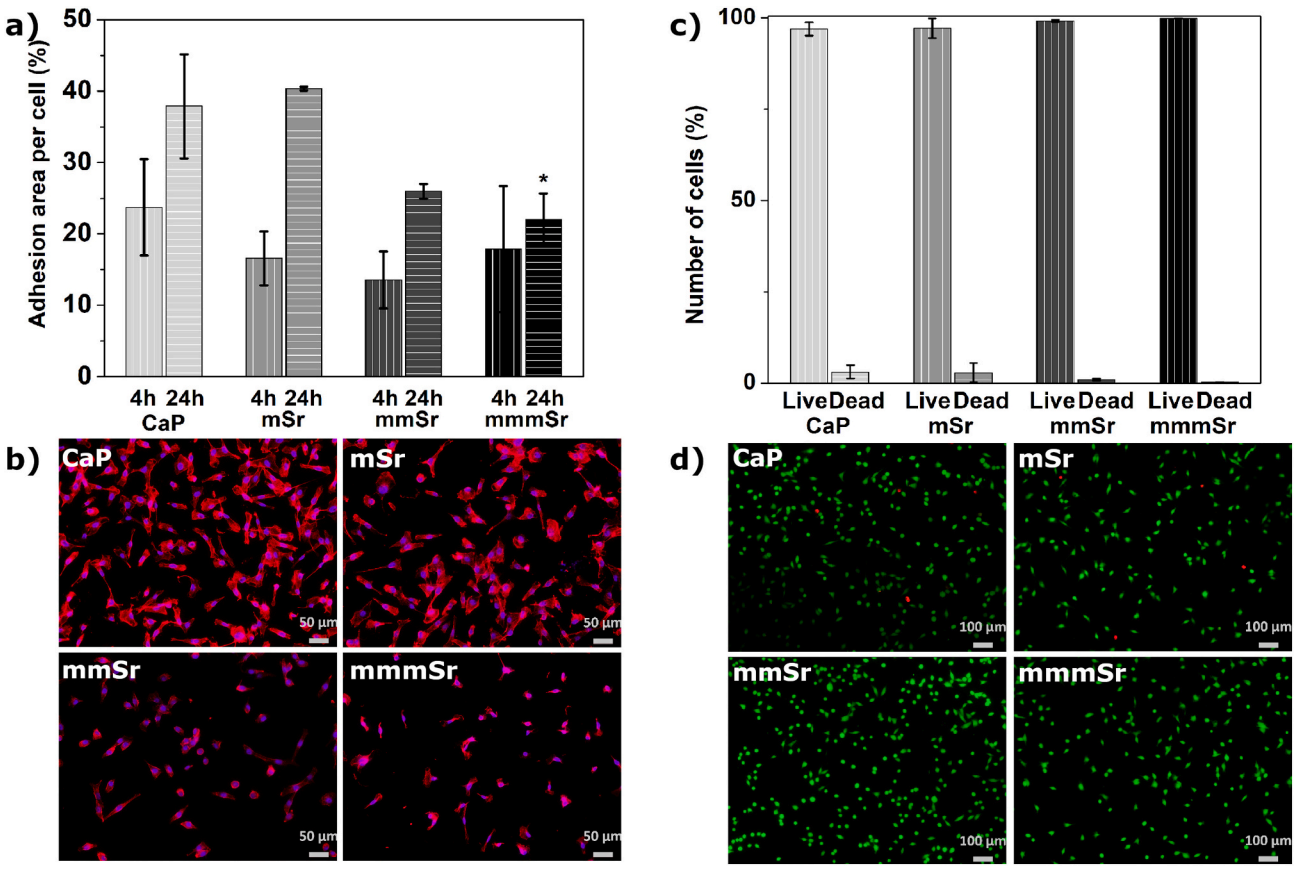

Fig. 3. a) Adhesion area (%) of MG-63 cells cultured for 4 and 24 h (*$p < 0.05$ indicates a significant difference compared with the mSr 24 h) and b) fluorescence images of MG-63 cells cultured after 24 h with F-actin stained with Phalloidin in red and the cell nuclei stained with DAPI in blue; c) Number of live and dead cells (%) and d) fluorescence images of LIVE/DEAD® staining of MG-63 cells after 24 h of incubation. (For interpretation of the references to color in this figure legend, the reader is referred to the web version of this article.)

anatase phase, behaviour that was not observed in the rutile phases structures. In this way, probably the poor osteoblast adhesion on mmmSr may be due to the combined action of higher amount of Sr and rutile phase that can possibly compromise cell adhesion. Ribeiro et al. [9] previously reported the interface osteoblast/CaP cross-section after 2 h of osteoblast adhesion and showed that cells are well adhered to the surface when the amorphous nanometric film rich and Ca and P is present, but not when the surface is made of a mixture of rutile and amorphous phases. The authors presented a TEM image of the cross-section showing that the inner part of the oxide was composed of a mixture of crystalline and amorphous structures, while the top of the oxide was mainly composed of an amorphous phase rich in Ca and P that enter in direct contact with cells stimulating their adhesion [19].

Osteoblastic-like cells adhered to the oxide layers were viable, indicating that although higher concentrations of Sr compromise cell adhesion their viability was not disturbed (see Fig. 3c–d). These results are consistent with the literature where no appreciable Sr effects on pre-osteoblastic [45] and mesenchymal stem [68] cells cytotoxicity were reported. MAO surfaces are extremely porous and rough which can mislead the cell density on different fields due to the peculiarity ridges and valleys present on the surfaces.

Osteoblast morphology was examined by SEM after 4 h, 24 h and 21 days of culture (Fig. 4). No significant differences were seen in cell morphologies between all the conditions and between the studied time-points. According to the results presented in Fig. 4c and d, osteoblasts on Ca-P-Sr TiO_2 porous layer were well attached to their surfaces. It was also possible to see osteoblasts spreading on the surface, with extended filopodia covering the porous oxide surface, attached to the edges of the pores, penetrating and crossing the pores (see Fig. 4a–f after 4 and 24 h). After 21 days, osteoblasts continued to be well-adhered to the oxide layer and it was possible to observe a thin lamellipodia on the top of some parts of the oxide layer, with cell processes extending over other neighbouring cells indicated the formation of cell monolayer (Fig. 4g). No differences were obtained in the cell morphology between all the conditions after 21 days of incubation. On the other hand, superficial and cross-sectional observations of the cell/oxide layer interface revealed osteoblasts penetration in the pores, as illustrated on Fig. 4i.

Bone is a living organ maintained by living cells such as osteoblasts, osteoclasts, osteocytes among others. It is composed by an inorganic component that is predominantly hydroxyapatite ($Ca_5(PO_4)_3(OH)$) and an organic matrix of type I collagen and small quantities of osteonectin and osteocalcin that promote bone regeneration [69–72]. Bone mineralization is the result of complex biological processes in which deposition of inorganic salts is induced by a template of collagen type I network. Collagen provides the template for mineral deposition, where the size and the organization of the collagen fibrils determine the dimensions that mineral crystals can attain [69–72]. Fig. 5a presents the fluorescence microscope images of MG-63 cells cultured after 21 days (stained with DAPI for nucleus, phalloidin for actin and collagen type I for collagen secretion) where it was possible to observe the presence of collagen network in all conditions. Fig. 5b shows the results of the semi-quantitative analysis of collagen deposition, where a statistically significant increase on collagen secretion was observed in mmSr and mmmSr conditions compared with the control group. Previous studies using Sr for other applications showed that Sr was promoting the collagen secretion [73]. Naruphontjirakul et al. [73] evaluated the biological behaviour of human stem cells on bioactive glass and the biological effect of Sr ions released. The presence of Sr-bioactive glass

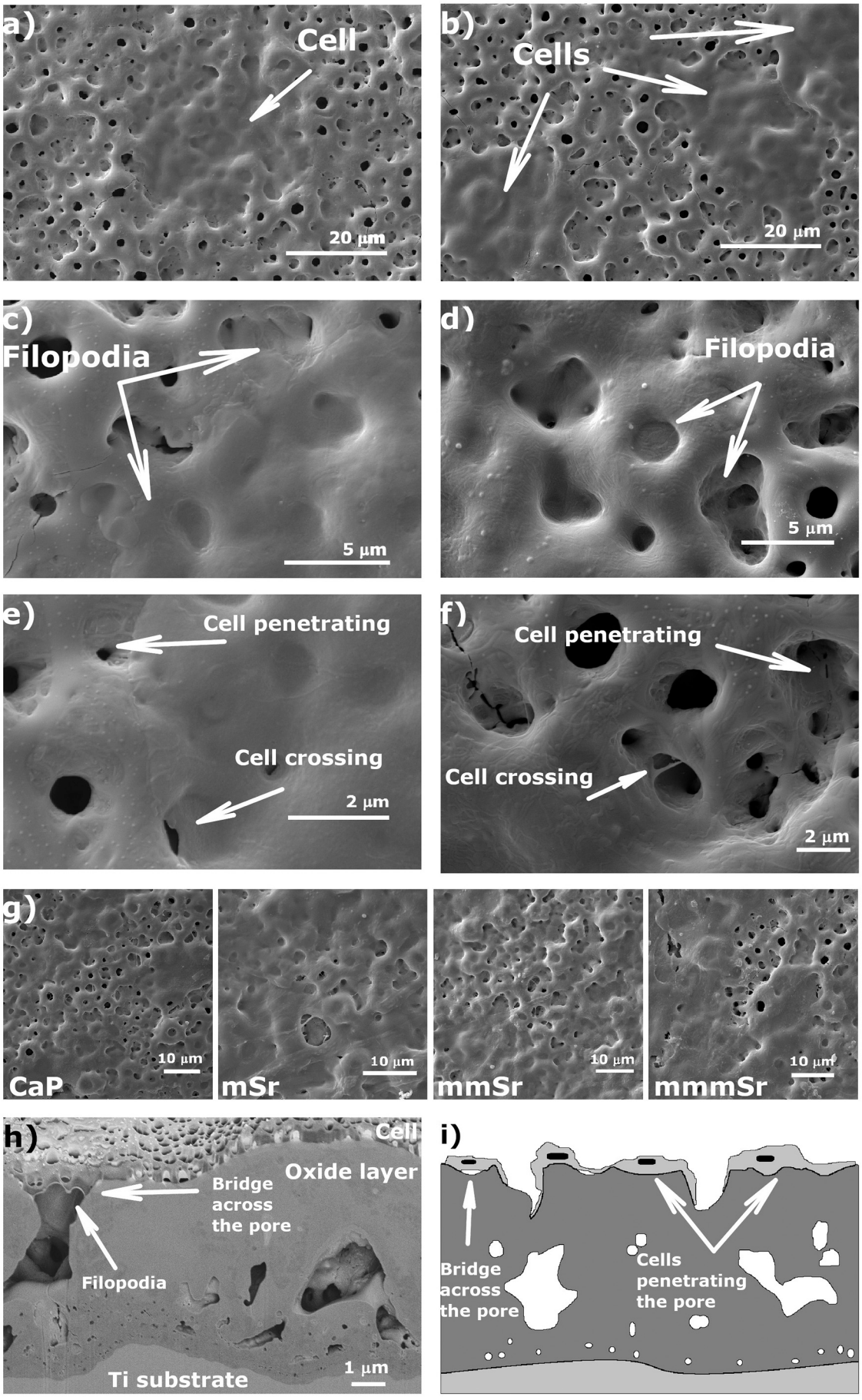

(caption on next page)

Fig. 4. SE-SEM images presenting cell morphology after a, c and e) 4 h of seeding, and b), d) and f) 24 h of seeding; g) SE-SEM images presenting cell morphology after 21 days of culture; h) SE-SEM image of the cross-section of the oxide layer with a cell on top 24 h after seeding; i) illustration of the interface between cells and the oxide layer [figures a, c, e, f and h are from mmmSr condition, b from mSr condition and d from mmSr condition. No significant differences were seen in cell adhesion morphologies by SEM analysis between the studied conditions and time-points].

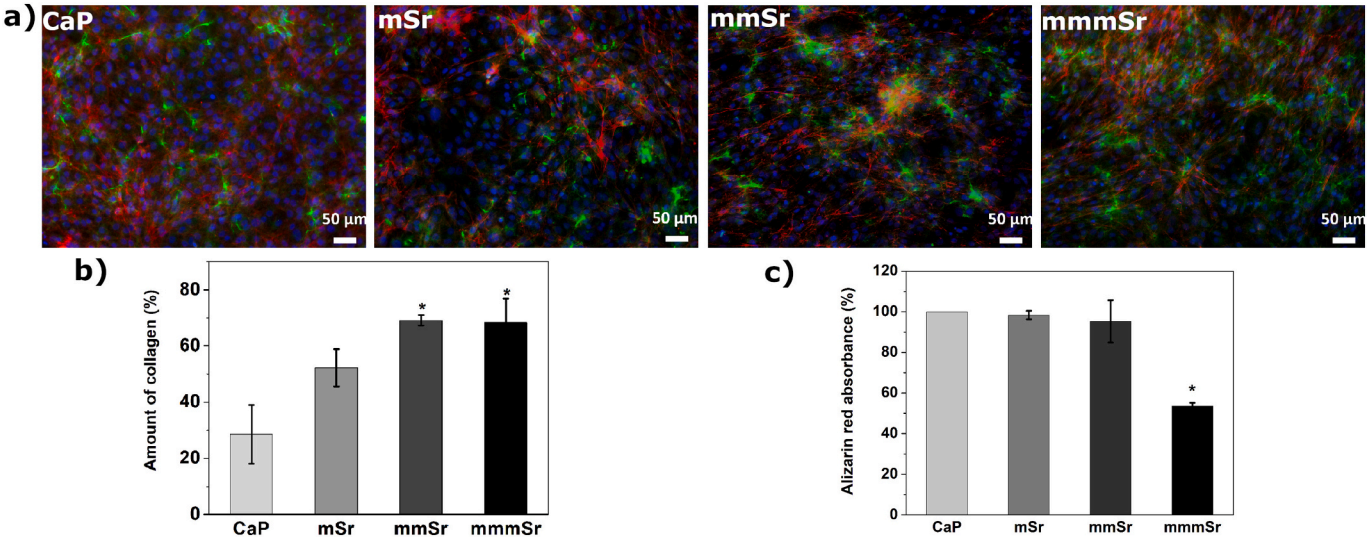

Fig. 5. a) Fluorescence images of MG-63 cells cultured after 21 days with F-actin stained with Phalloidin in red, the cell nuclei stained with DAPI in blue and collagen stained in green and b) amount of collagen (%) of MG-63 cells cultured for 21 days (*$p < 0.05$ indicates a significant difference compared with the CaP); c) quantitative mineralization results of alizarin red-s absorbance (%) after 21 days of incubation (*$p < 0.05$ indicates a significant difference compared with the CaP, mSr and mmmSr). (For interpretation of the references to color in this figure legend, the reader is referred to the web version of this article.)

induced a higher amount of mature extracellular matrix formation and expression of proteins associated with collagen production.

Alizarin red-s was used to stain matrix calcium-phosphates deposits and results presented in Fig. 5c. As it is possible to observe a clear statistically significant decrease in the amount of calcium deposits was observed for the mmmSr group. It is possible that the combined action of higher content of Sr with rutile phase, can be what is delaying the mineralization process. Previously, Verberckmoes et al. [74] showed a multiphasic interference of Sr ions with osteoblast cells mineralization. Particularly, it was shown by the authors that a Sr dose between 2 and 5 ppm was promoting cell mineralization, while a Sr dose between 20 and 100 ppm showed the opposite effect. Studies [39,75,76] indicated that Sr ions can activate signalling pathways particularly, through a calcium-sensing receptor, stimulating or inhibit cell mineralization. On the other hand, Xu et al. [38] showed that higher amount of Sr presented an adverse effect on the osteogenic function of bone marrow mesenchymal stem cells and reported that more amount of rutile might be influencing their mineralization.

Interestingly, the group with a higher amount of Sr showed higher secretion of collagen matrix despite the decrease in mineralization processes. Mineralization of calcium phosphates in bone has been proposed to proceed through an initial collagen secretion and deposition of the mineralized matrix *via* amorphous precursor phase which transforms into nanocrystalline hydroxyapatite [77–79]. Possibly, the higher amount of Sr can be delaying the mineralization process. Another possibility is that the surface with a higher amount of Sr is inducing a mineralization process with a deficient HAP structure, and/or an amorphous precipitate as stated by Verberckmoes et al. [80]. The authors showed that low Sr amount did not affect neither HAP crystal solubility nor mineralization. On the contrary, when the Sr content increased, a physicochemical interference of Sr in the HAP formation was observed resulting in defective mineralization. The authors presented an XRD of the deposited mineral that revealed a diffuse pattern, characteristic for a non-crystalline (amorphous) HAP precipitate [80].

The mineralization and differentiation of osteoblasts are processes regulated by complex interactions among different molecules like hormones, cytokines and local growth factors, among others. The cytokines secretion plays a crucial role in bone remodelling since these factors appear to have crucial roles in both normal and pathologic bone cell functions [81,82]. The amount of the cytokines, chemokines and growth factors were quantified in the supernatant after 21 days of cell culture and results are presented in Fig. 6. Although almost 30 soluble secreted mediators were quantified, it was only observed significant differences in interleukin-1 receptor antagonist (IL-1Ra), granulocyte colony-stimulating factor (G-CSF) ad IL-15 cytokines.

Comparing with CaP control surfaces, mSr and mmmSr groups promoted reduced secretion levels of IL-1Ra, whereas mmSr increased its levels. IL-1Ra is a member of the IL-1 family involved in modulation of immune and inflammatory responses. In specific events where IL-1 β levels are increased in the microenvironment, the reduction of IL-1Ra levels leads to a greater IL-1β ability that activates its signalling cascades and induces inflammation [83–85]. Indeed, increased levels of IL-1Ra have been associated with the inhibition of bone formation *in vivo* [86]. In this sense, our data suggested that mmSr possibly induce inhibition of bone formation and that mSr and mmmSr could turn the microenvironment more susceptible to inflammation. However, in a complex system, several secreted proteins are able to promote a balance in order to maintain homeostasis.

Lower amount of Sr (mSr) on the oxide layer seemed to induce the secretion of higher levels of G-CSF, whereas higher amount of Sr (mmSr and mmmSr) do not alter G-CSF levels, being comparable to control group CaP. G-CSF is considered an endogenous hematopoietic growth factor that induces proliferation, differentiation, and release of neutrophils from bone marrow [87]. Despite these relevant effects, overexpression of G-CSF may also lead to bone resorption in mice [88]. Resuming mSr induced the secretion of G-CSF that is an important growth factor that stimulates the bone marrow to produce stem cells and releases them into the bloodstream stimulating osteogenesis [89].

Regarding the cytokine IL-15, mmSr promote its increase in secretion, but not mSr and mmmSr. IL-15 is widely known for its role in

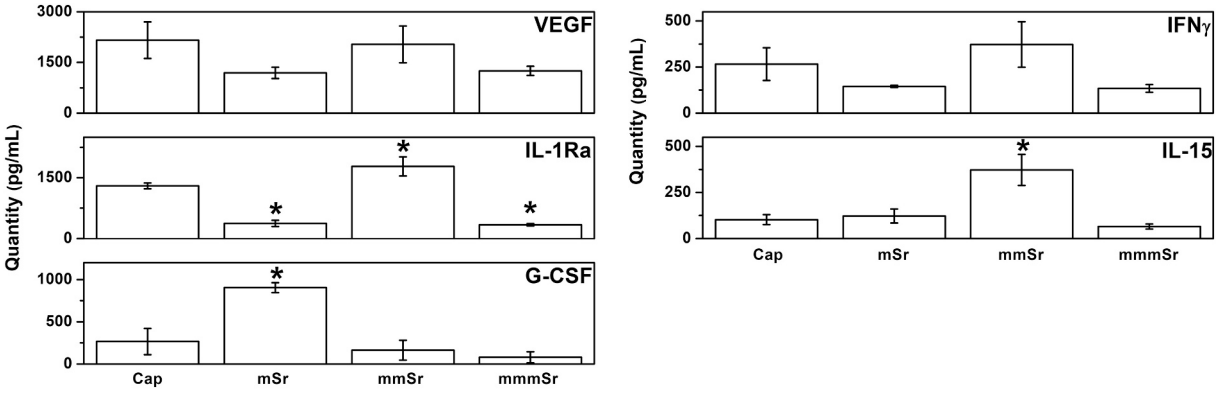

Fig. 6. VEGF, IL-1Ra, G-CSF, IFNy, IL-15 and bFGF cytokines secreted by osteoblasts after 21 days of incubation (*$p < 0.05$ indicates a significant difference compared with the CaP).

osteoclast differentiation [82] and consequent osteoclastogenesis [81,88]. Possibly the reduced secretion of this cytokine for mSr and mmmSr indicates that these surfaces inhibit osteoclastogenesis.

All the surfaces induced osteoblasts to secrete vascular endothelial growth factor (VEGF) and interferon gamma (IFN-y) since no significant differences were observed when comparing to CaP. VEGF, a potent mediator of angiogenesis displaying an important role in bone development and regeneration [72,90], and IFN-y, with variable effects on many immunological functions as well as in inflammation, seemed to have a similar secretion pattern between groups. In bone, studies showed that IFN-γ plays an important role in bone homeostasis and increases alkaline phosphatase activity in osteoblast-like cells. However, it also plays important roles in osteoclastogenesis [91]. So, depending on the circumstances, IFN-y may contribute to a reduce inflammation but also may promote bone resorption and formation [9,82,87,88,92].

Resuming, mSr and mmmSr induced the secretion of lower levels of IL-1Ra, with mSr inducing G-CSF secretion. In addition, mmSr induced increased levels of IL-1Ra and seemed to increase IL-15 secretion. It is important to disclose that increased levels of a secreted protein in mSr experimental group do not mean that mmSr or mmmSr (or *vice-versa*) would result in its increased levels in a concentration dependent manner. Eukaryotic cells display different mechanisms for maintaining their microenvironment balance. Then, it is common that the challenged cells respond, altering the levels of many secreted proteins and activating or deactivating intracellular signalling pathways, always searching for survival and homeostasis. It is conceivable that it was occurring in this study. Taken together, our data suggested that although mSr surfaces possibly secrete cytokines involved in inflammation they also secrete growth factors that contribute to osteogenesis and other cytokines that inhibit osteoclast formation and consequent bone resorption.

This work gives an insight into the effect of Sr amount in the oxide layer on osteoblast culture. It is shown that the presence of Sr, with a dose-depending effect, influences the behaviour of osteoblast adhesion, mineralization and cytokines released. Sr is a unique element showing promising results in its dual action in the bone cells, osteoblast and osteoclasts. So, as future work, the effect of Sr amount on osteoclast behaviour should be evaluated. The real magnitude of the effect of Sr amount cannot be easily evaluated, and there may be some synergistic relationships coming into account, mainly between osteoblast and osteoclast independent and dependent responses. The optimal material that will promote the enhancement of bone formation osseointegration as well as a reduction of bone resorption should be a result of the synergistic effect exerted by the hierarchical surface topography (micro- and nano-porous), chemical composition (TiO_2 with Ca-P-Sr) and crystal structure (anatase + rutile) together, and as it was studied and presented, the amount of Sr can be in the range of mSr and mmSr groups.

4. Conclusion

This study has outlined the effect of the Sr amount in porous Ca- and P-rich TiO_2 layers processed by MAO, evaluated in terms of surface characteristics and *in vitro* biological response. Incorporation of Sr did not affect the pore size and morphology in the TiO_2 layer, although, changed the chemical composition and the oxide crystal structure. Cell viability was not compromised, however, the combination of higher amount of Sr with the higher amount of rutile impaired osteoblast adhesion, induced collagen secretion and mineralization compromised. Possibly Sr is delaying the mineralization process or inducing the formation of a deficient HAP structure. More studies are necessary to clarify these phenomena however we can conclude that lower amount of Sr presented an overall good biological outcome which is likely to be a beneficial surface to be used as implants and other bone regeneration applications.

Supplementary data to this article can be found online at https://doi.org/10.1016/j.msec.2020.111735.

CRediT authorship contribution statement

Author's detailed description of their diverse contributions to the published work are given below:

A.I. Costa: Conceptualization (equal), Methodology (equal), Validation (equal), Formal analysis (lead), Investigation (lead), Writing - original draft (lead), Visualization (lead).
S. Gemini-Piperni: Methodology (equal), Validation (equal), Formal analysis (equal), Investigation (lead), Writing - review & editing (supporting).
A.C. Alves: Conceptualization (equal), Methodology (equal), Validation (supporting), Formal analysis (supporting).
N.A. Costa: Methodology (supporting).
N.R. Checca: Methodology (supporting).
P.E. Leite: Methodology (supporting), Resources (supporting).
L.A. Rocha: Writing - review & editing (supporting), Supervision (supporting), Funding acquisition (lead).
A.M.P. Pinto: Validation (supporting), Formal analysis (supporting), Resources (supporting).
F. Toptan: Conceptualization (lead), Methodology (equal), Validation (equal), Formal analysis (equal), Writing - review & editing (lead), Supervision (lead), Project administration (lead), Funding acquisition (lead).
A.L. Rossi: Methodology (equal), Validation (equal), Resources (supporting), Supervision (supporting).
A.R. Ribeiro: Methodology (equal), Validation (equal), Formal analysis (equal), Resources (supporting), Writing - review & editing (lead), Supervision (lead).

All authors discussed the results and contributed to the final manuscript.

Declaration of competing interest

The authors declare that they have no known competing financial interests or personal relationships that could have appeared to influence the work reported in this paper.

Acknowledgments

This work was supported by FCT with the reference projects UID/EEA/04436/2019, M-ERA-NET/0001/2015 and FCT/CAPES Procs.° 4.4.1.00. Also the support of FAPESP is acknowledged (Proc. 2017/24300-4). A.I. Costa is very grateful for the PhD grant through NORTE-08-5369-FSE-000051 project. The authors would like to thank the LABNANO/CBPF and Centro Nacional de Biologia Estrutural e Bioimagem (Cenabio) in Rio de Janeiro for technical support during electron microscopy work.

References

[1] OECD, Health at a Glance 2017: OECD Indicators, 2017 (Paris).
[2] R.J. Ferguson, A.J. Palmer, A. Taylor, M.L. Porter, H. Malchau, S. Glyn-Jones, Hip and knee replacement 1 - hip replacement, Lancet. 392 (2018) 1662–1671.
[3] J.T. Evans, J.P. Evans, R.W. Walker, A.W. Blom, M.R. Whitehouse, A. Sayers, How long does a hip replacement last? A systematic review and meta-analysis of case series and national registry reports with more than 15 years of follow-up, Lancet. 393 (2019) 647–654.
[4] M. Bruschi, D. Steinmüller-Nethl, W. Goriwoda, M. Rasse, Composition and modifications of dental implant surfaces, J. Oral Implant. (2015) 1–14.
[5] M. Geetha, A.K. Singh, R. Asokamani, A.K. Gogia, Ti based biomaterials, the ultimate choice for orthopaedic implants – a review, Prog. Mater. Sci. 54 (2009) 397–425.
[6] H.J. Rack, J.I. Qazi, Titanium alloys for biomedical applications, Mater. Sci. Eng. C. 26 (2006) 1269–1277.
[7] A.C. Alves, R. Thibeaux, F. Toptan, A.M.P. Pinto, P. Ponthiaux, B. David, Impact of bio-functionalization on NIH/3T3 adhesion, proliferation and osteogenic differentiation of MC3T3-E1 over highly porous titanium implant material, J. Biomed. Mater. Res. Part B - Appl. Biomater. 107 (2019) 73–85.
[8] L. Xu, K. Zhang, C. Wu, X. Lei, J. Ding, X. Shi, C. Liu, Micro-arc oxidation enhances the blood compatibility of ultrafine-grained pure titanium, Materials (Basel). 10 (2017) 1446.
[9] A.R. Ribeiro, F. Oliveira, L.C. Boldrini, P.E. Leite, P. Falagan-Lotsch, A.B. R. Linhares, W.F. Zambuzzi, B. Fragneaud, A.P.C. Campos, C.P. Gouvêa, B. S. Archanjo, C.A. Achete, E. Marcantonio, L.A. Rocha, J.M. Granjeiro, Micro-arc oxidation as a tool to develop multifunctional calcium-rich surfaces for dental implant applications, Mater. Sci. Eng. C. 54 (2015) 196–206.
[10] Y. Wang, H. Yu, C. Chen, Z. Zhao, Review of the biocompatibility of micro-arc oxidation coated titanium alloys, Mater. Des. 85 (2015) 640–652.
[11] I.S. Park, T.G. Woo, W.Y. Jeon, H.H. Park, M.H. Lee, T.S. Bae, K.W. Seol, Surface characteristics of titanium anodized in the four different types of electrolyte, Electrochim. Acta 53 (2007) 863–870.
[12] M.D. Roach, R.S. Williamson, I.P. Blakely, L.M. Didier, Tuning anatase and rutile phase ratios and nanoscale surface features by anodization processing onto titanium substrate surfaces, Mater. Sci. Eng. C. 58 (2016) 213–223.
[13] D. Velten, V. Biehl, F. Aubertin, B. Valeske, W. Possart, J. Breme, Preparation of TiO2 layers on cp-Ti and Ti6Al4V by thermal and anodic oxidation and by sol-gel coating techniques and their characterization, J. Biomed. Mater. Res. 59 (2002) 18–28.
[14] M. Fazel, H.R. Salimijazi, M.A. Golozar, M.R. Garsivaz jazi, A comparison of corrosion, tribocorrosion and electrochemical impedance properties of pure Ti and Ti6Al4V alloy treated by micro-arc oxidation process, Appl. Surf. Sci. 324 (2015) 751–756.
[15] D. Quintero, O. Galvis, J.A. Calderón, J.G. Castaño, F. Echeverría, Control of the physical properties of anodic coatings obtained by plasma electrolytic oxidation on Ti6Al4V alloy, Surf. Coatings Technol. 283 (2015) 210–222.
[16] L. Benea, E. Mardare-Danaila, M. Mardare, J.-P. Celis, Preparation of titanium oxide and hydroxyapatite on Ti–6Al–4V alloy surface and electrochemical behaviour in bio-simulated fluid solution, Corros. Sci. 80 (2014) 331–338.
[17] A.C. Alves, F. Oliveira, F. Wenger, P. Ponthiaux, J.-P. Celis, L.A. Rocha, Tribocorrosion behaviour of anodic treated titanium surfaces intended for dental implants, J. Phys. D. Appl. Phys. 46 (2013) 404001.
[18] I. da S.V. Marques, M.F. Alfaro, N.C. da Cruz, M.F. Mesquita, C. Sukotjo, M.T. Mathew, V.A.R. Barão, Tribocorrosion behavior of biofunctional titanium oxide films produced by micro-arc oxidation: synergism and mechanisms, J. Mech. Behav. Biomed. Mater. 60 (2016) 8–21.
[19] F.G. Oliveira, A.R. Ribeiro, G. Perez, B.S. Archanjo, C.P. Gouvea, J.R. Araújo, A.P. C. Campos, A. Kuznetsov, C.M. Almeida, M.M. Maru, C.A. Achete, P. Ponthiaux, J.-P. Celis, L.A. Rocha, Understanding growth mechanisms and tribocorrosion behaviour of porous TiO2 anodic films containing calcium, phosphorous and magnesium, Appl. Surf. Sci. 341 (2015) 1–12.
[20] L. Benea, E. Danaila, P. Ponthiaux, Effect of titania anodic formation and hydroxyapatite electrodeposition on electrochemical behaviour of Ti-6Al-4V alloy under fretting conditions for biomedical applications, Corros. Sci. 91 (2015) 262–271.
[21] F. Toptan, A.C. Alves, A.M.P. Pinto, P. Ponthiaux, Tribocorrosion behavior of bio-functionalized highly porous titanium, J. Mech. Behav. Biomed. Mater. 69 (2017) 144–152.
[22] Z.S. Tao, W.S. Zhou, X.W. He, W. Liu, B.L. Bai, Q. Zhou, Z.L. Huang, K.K. Tu, H. Li, T. Sun, Y.X. Lv, W. Cui, L. Yang, A comparative study of zinc, magnesium, strontium-incorporated hydroxyapatite-coated titanium implants for osseointegration of osteopenic rats, Mater. Sci. Eng. C. 62 (2016) 226–232.
[23] J. Zhou, L. Zhao, Multifunction Sr, Co and F co-doped microporous coating on titanium of antibacterial, angiogenic and osteogenic activities, Acta Biomater. 43 (2016) 358–368.
[24] K.C. Kung, T.M. Lee, T.S. Lui, Bioactivity and corrosion properties of novel coatings containing strontium by micro-arc oxidation, J. Alloys Compd. 508 (2010) 384–390.
[25] W. Zhang, H. Cao, X. Zhang, G. Li, Q. Chang, J. Zhao, Y. Qiao, X. Ding, G. Yang, X. Liu, X. Jiang, A strontium-incorporated nanoporous titanium implant surface for rapid osseointegration, Nanoscale. 8 (2016) 5291–5301.
[26] W. Liu, M. Cheng, T. Wahafu, Y. Zhao, H. Qin, J. Wang, X. Zhang, L. Wang, The in vitro and in vivo performance of a strontium-containing coating on the low-modulus Ti35Nb2Ta3Zr alloy formed by micro-arc oxidation, J. Mater. Sci. Mater. Med. 26 (2015) 203.
[27] X. Lin, X. Yang, L. Tan, M. Li, X. Wang, Y. Zhang, K. Yang, Z. Hu, J. Qiu, In vitro degradation and biocompatibility of a strontium-containing micro-arc oxidation coating on the biodegradable ZK60 magnesium alloy, Appl. Surf. Sci. 288 (2014) 718–726.
[28] M. Pilmane, K. Salma-Ancane, D. Loca, J. Locs, L. Berzina-Cimdina, Strontium and strontium ranelate: historical review of some of their functions, Mater. Sci. Eng. C. 78 (2017) 1222–1230.
[29] K.C. Kung, T.M. Lee, J.L. Chen, T.S. Lui, Characteristics and biological responses of novel coatings containing strontium by micro-arc oxidation, Surf. Coatings Technol. 205 (2010) 1714–1722.
[30] G. Boivin, P. Deloffre, B. Perrat, G. Panczer, M. Boudeulle, Y. Tsouderos, P. J. Meunier, Strontium distribution and interreactions with bone mineral in male monkey iliac bone after strontium salt (S 12911) administration, Osteoporos. Int. 6 (1996) 1302–1311.
[31] C. Chung, H. Long, Systematic strontium substitution in hydroxyapatite coatings on titanium via micro-arc treatment and their osteoblast/osteoclast responses, Acta Biomater. 7 (2011) 4081–4087.
[32] L. Yin, J. Zhou, L. Gao, C. Zhao, J. Chen, X. Lu, J. Wang, J. Weng, B. Feng, Characterization and osteogenic activity of SrTiO3/TiO2 nanotube heterostructures on microporous titanium, Surf. Coat. Technol. 330 (2017) 121–130.
[33] Q. Zhao, L. Yi, L. Jiang, Y. Ma, H. Lin, J. Dong, Surface functionalization of titanium with zinc/strontium-doped titanium dioxide microporous coating via microarc oxidation, Nanomedicine NBM. 16 (2019) 149–161.
[34] M. Khodaei, A. Valanezhad, I. Watanabe, Controlled gentamicin- strontium release as a dual action bone agent: combination of the porous titanium scaffold and biodegradable polymers, J. Alloys Compd. 720 (2017) 22–28.
[35] J. Yan, J. Sun, P.K. Chu, Y. Han, Y. Zhang, Bone integration capability of a series of strontium-containing hydroxyapatite coatings formed by micro-arc oxidation, J Biomed Mater Res Part A. 101A (2013) 2465–2480.
[36] J. Wen, J. Li, H. Pan, W. Zhang, D. Zeng, L. Xu, Q. Wu, X. Zhang, X. Liu, X. Jiang, Strontium delivery on topographical titanium to enhance bioactivity and osseointegration in osteoporotic rats, J. Mater. Chem. B 3 (2015) 4790–4804.
[37] D. Bellucci, V. Cannillo, A. Anesi, R. Salvatori, L. Chiarini, T. Manfredini, D. Zaffe, Bone regeneration by novel bioactive glasses containing strontium and/or magnesium: a preliminary in-vivo study, Materials (Basel). 11 (2018) 2223.
[38] Z. Xu, H. Lu, J. Lu, C. Lv, G. Wang, Enhanced osteogenic activity of Ti alloy implants by modulating strontium configuration in their surface oxide layers, RSC Adv. 8 (2018) 3051–3060.
[39] P.J. Marie, P. Ammann, G. Boivin, C. Rey, Mechanisms of action and therapeutic potential of strontium in bone, Calcif. Tissue Int. 69 (2001) 121–129.
[40] T.-M. Lee, K.-C. Kung, T.-S. Lui, Characteristics and biological responses of novel coatings containing strontium by micro-arc oxidation, Weather. (2005) 1–8.
[41] J.-W. Park, Increased bone apposition on a titanium oxide surface incorporating phosphate and strontium, Clin. Oral Impl. Res. 22 (2011) 230–234.
[43] Z. Zhang, Osteoblastic cell adhesion on strontium- incorporated porous nanostructured TiO2 coating prepared by micro-arc oxidation, J. Clin. Exp. Orthop. 1 (2015) 1–7.
[44] M. Sato, P. Chen, Y. Tsutsumi, M. Shiota, T. Hanawa, S. Kasugai, Effect of strontium ions on calcification of preosteoblasts cultured on porous calcium- and phosphate-containing titanium oxide layers formed by micro-arc oxidation, Dent. Mater. J. 35 (2016) 627–634.
[45] X. He, X. Zhang, L. Bai, R. Hang, X. Huang, L. Qin, X. Yao, B. Tang, Antibacterial ability and osteogenic activity of porous Sr/Ag-containing TiO2 coatings, Biomed. Mater. 11 (2016), 045008.
[46] K.-C. Kung, K. Yuan, T.-M. Lee, T.-S. Lui, Effect of heat treatment on microstructures and mechanical behavior of porous Sr–Ca–P coatings on titanium, J. Alloys Compd. 515 (2012) 68–73.

[47] H. Xie, Z. Gu, Y. He, J. Xu, C. Xu, L. Li, Q. Ye, Microenvironment construction of strontium-calcium-based biomaterials for bone tissue regeneration: the equilibrium effect of calcium to strontium, J. Mater. Chem. B 6 (2018) 2332–2339.
[49] A.C. Alves, F. Wenger, P. Ponthiaux, J.-P. Celis, A.M. Pinto, L.A. Rocha, J.C. S. Fernandes, Corrosion mechanisms in titanium oxide-based films produced by anodic treatment, Electrochim. Acta 234 (2017) 16–27.
[50] A.E.R. Friedemann, T.M. Gesing, P. Plagemann, Electrochemical rutile and anatase formation on PEO surfaces, Surf. Coatings Technol. 315 (2017) 139–149.
[51] J.I. Rosales-Leal, M.A. Rodríguez-Valverde, G. Mazzaglia, P.J. Ramón-Torregrosa, L. Díaz-Rodríguez, O. García-Martínez, M. Vallecillo-Capilla, C. Ruiz, M. A. Cabrerizo-Vílchez, Effect of roughness, wettability and morphology of engineered titanium surfaces on osteoblast-like cell adhesion, Colloids Surfaces A Physicochem. Eng. Asp. 365 (2010) 222–229.
[52] O. Banakh, T. Journot, P.A. Gay, J. Matthey, C. Csefalvay, O. Kalinichenko, O. Sereda, M. Moussa, S. Durual, L. Snizhko, Synthesis by anodic-spark deposition of Ca- and P-containing films on pure titanium and their biological response, Appl. Surf. Sci. 378 (2016) 207–215.
[53] L. Wang, G.H. Nancollas, Calcium orthophosphates: crystallization and dissolution, Chem. Rev. 108 (2008) 4628–4669.
[54] S. Kim, H. Ryu, H. Shin, H.S. Jung, K.S. Hong, In situ observation of hydroxyapatite nanocrystal formation from amorphous calcium phosphate in calcium-rich solutions, Mater. Chem. Phys. 91 (2005) 500–506.
[55] Y. Lu, P. Wan, L. Tan, B. Zhang, K. Yang, J. Lin, Preliminary study on a bioactive Sr containing Ca-P coating on pure magnesium by a two-step procedure, Surf. Coat. Technol. 252 (2014) 79–86.
[56] G. Mortazavi, J. Jiang, E.I. Meletis, Investigation of the plasma electrolytic oxidation mechanism of titanium, Appl. Surf. Sci. 488 (2019) 370–382.
[57] D.A.H. Hanaor, C.C. Sorrell, Review of the anatase to rutile phase transformation, J. Mater. Sci. 46 (2011) 855–874.
[58] N. Wetchakun, S. Phanichphant, Effect of temperature on the degree of anatase-rutile transformation in titanium dioxide nanoparticles synthesized by the modified sol-gel method, Curr. Appl. Phys. 8 (2008) 343–346.
[59] L.P. Qiao, J. Lou, S.F. Zhang, B. Qu, W.H. Chang, R.F. Zhang, The entrance mechanism of calcium and phosphorus elements into micro arc oxidation coatings developed on Ti6Al4V alloy, Surf. Coatings Technol. 285 (2016) 187–196.
[60] S.A. Alves, A.R. Ribeiro, S. Gemini-Piperni, R.C. Silva, A.M. Saraiva, P.E. Leite, G. Perez, S.M. Oliveira, J.R. Araujo, B.S. Archanjo, M.E. Rodrigues, M. Henriques, J.P. Celis, T. Shokuhfar, R. Borojevic, J.M. Granjeiro, L.A. Rocha, TiO2 nanotubes enriched with calcium, phosphorous and zinc: promising bio-selective functional surfaces for osseointegrated titanium implants, RSC Adv. 7 (2017) 49720–49738.
[61] G.C. Gomes, F.F. Borghi, R.O. Ospina, E.O. López, F.O. Borges, A. Mello, Nd:YAG (532 nm) pulsed laser deposition produces crystalline hydroxyapatite thin coatings at room temperature, Surf. Coatings Technol. 329 (2017) 174–183.
[62] E.O. López, A. Mello, M. Farina, A.M. Rossi, A.L. Rossi, Nanoscale analysis of calcium phosphate films obtained by RF magnetron sputtering during the initial stages of deposition, Surf. Coatings Technol. 279 (2015) 16–24.
[63] Y. Huang, X. Zhang, H. Zhang, H. Qiao, X. Zhang, T. Jia, S. Han, Y. Gao, H. Xiao, H. Yang, Fabrication of silver- and strontium-doped hydroxyapatite/TiO 2 nanotube bilayer coatings for enhancing bactericidal effect and osteoinductivity, Ceram. Int. 43 (2017) 992–1007.
[64] Q. Liu, J. Li, Z. Zhou, J. Xie, J.Y. Lee, Hydrophilic mineral coating of membrane substrate for reducing internal concentration polarization (ICP) in forward osmosis, Sci. Rep. 6 (2016) 1–10.
[65] S. Yamaguchi, S. Nath, T. Matsushita, T. Kokubo, Controlled release of strontium ions from a bioactive Ti metal with a Ca-enriched surface layer, Acta Biomater. 10 (2014) 2282–2289.
[66] M.C. Biesinger, B.P. Payne, A.P. Grosvenor, L.W.M. Lau, A.R. Gerson, R.S.C. Smart, Resolving surface chemical states in XPS analysis of first row transition metals, oxides and hydroxides: Cr, Mn, Fe, Co and Ni, Appl. Surf. Sci. 257 (2011) 2717–2730.
[67] J. He, E. Zhou, X. Zhou, X. Zhong, X. Zhang, P. Wan, B. Zhu, W. Chen, The anatase phase of nanotopography titania plays an important role on osteoblast cell morphology and proliferation, J Mater Sci Mater Med. 19 (2008) 3465–3472.
[68] S. Wang, R. Li, L. Dong, Z.-Y. Zhang, G. Liu, H. Liang, Y. Qin, J. Yu, Y. Li, Fabrication of bioactive 3D printed porous titanium implants with Sr ions-incorporated zeolite coatings for bone ingrowth, J. Mater. Chem. B 6 (2018) 3254–3261.
[69] F. Yang, D. Yang, J. Tu, Q. Zheng, L. Cai, L. Wang, Strontium enhances osteogenic differentiation of mesenchymal stem cells and in vivo bone formation by activating Wnt/catenin signaling, Stem Cells 29 (2011) 981–991.
[70] P. Proff, P. Römer, The molecular mechanism behind bone remodelling: a review, Clin. Oral Investig. 13 (2009) 355–362.
[71] A. Nather, H.J.C. Ong, Z. Aziz, Structure of bone, in: Bone Grafts Bone Substitutes, World Scientific Publishing Co Pte Ltd., 2005: pp. 3–17.
[72] H.C. Blair, Q.C. Larrouture, Y. Li, H. Lin, D. Beer-Stoltz, L. Liu, R.S. Tuan, L. J. Robinson, P.H. Schlesinger, D.J. Nelson, Osteoblast differentiation and bone matrix formation in vivo and in vitro, Tissue Eng. Part B Rev. 23 (2017) 268–280.
[73] P. Naruphontjirakul, O. Tsigkou, S. Li, A.E. Porter, J.R. Jones, Human mesenchymal stem cells differentiate into an osteogenic lineage in presence of strontium containing bioactive glass nanoparticles, Acta Biomater. 90 (2019) 373–392.
[74] S.C. Verberckmoes, M.E. De Broe, P.C. D'Haese, Dose-dependent effects of strontium on osteoblast function and mineralization, Kidney Int. 64 (2003) 534–543.
[75] N. Chattopadhyay, S.J. Quinn, O. Kifor, C. Ye, E.M. Brown, The calcium-sensing receptor (CaR) is involved in strontium ranelate-induced osteoblast proliferation, Biochem. Pharmacol. 74 (2007) 438–447.
[76] J. Park, H. Kim, Y. Kim, J. Jang, H. Song, T. Hanawa, Osteoblast response and osseointegration of a Ti–6Al–4V alloy implant incorporating strontium, Acta Biomater. 6 (2010) 2843–2851.
[77] A. Lotsari, A.K. Rajasekharan, M. Halvarsson, M. Andersson, Transformation of amorphous calcium phosphate to bone-like apatite, Nat. Commun. 9 (2018).
[78] Y. Han, X. You, W. Xing, Z. Zhang, W. Zou, Paracrine and endocrine actions of bone - the functions of secretory proteins from osteoblasts, osteocytes, and osteoclasts, Bone Res. 6 (2018) 1–11.
[79] S. Boonrungsiman, E. Gentleman, R. Carzaniga, N.D. Evans, D.W. McComb, A. E. Porter, M.M. Stevens, The role of intracellular calcium phosphate in osteoblast-mediated bone apatite formation, Proc. Natl. Acad. Sci. U. S. A. 109 (2012) 14170–14175.
[80] S.C. Verberckmoes, G.J. Behets, L. Oste, A.R. Bervoets, L.V. Lamberts, M. Drakopoulos, A. Somogyi, P. Cool, W. Dorriné, M.E. De Broe, P.C. D'Haese, Effects of strontium on the physicochemical characteristics of hydroxyapatite, Calcif. Tissue Int. 75 (2004) 405–415.
[81] J.-M. Zhang, J. An, Cytokines, inflammation and pain, Int Anesth. Clin. 45 (2007) 27–37.
[82] M.C. Horowitz, J.A. Lorenzo, Local regulators of bone - IL-1, TNF, lymphotoxin, interferon-y, IL-8, IL-10, IL-4, the LIF/IL-6 Family, and additional cytokines, in: Princ, Second Edi, Academic Press, Bone Biol, 2002, pp. 961–977.
[83] P.E.C. Leite, M.R. Pereira, G. Harris, D. Pamies, L.M.G. Dos Santos, J.M. Granjeiro, H.T. Hogberg, T. Hartung, L. Smirnova, Suitability of 3D human brain spheroid models to distinguish toxic effects of gold and poly-lactic acid nanoparticles to assess biocompatibility for brain drug delivery, Part. Fibre Toxicol. 16 (2019) 1–20.
[84] J. Liao, C. Li, Y. Wang, M.H. Ten, X. Sun, A. Tian, Q. Zhang, X. Liang, Meta-analysis of the association between common interleukin-1 polymorphisms and dental implant failure, Mol. Biol. Rep. 41 (2014) 2789–2798.
[85] M. Hurme, S. Santtila, IL-1 receptor antagonist (IL-1Ra) plasma levels are co-ordinately regulated by both IL-1Ra and IL-1β genes, Eur. J. Immunol. 28 (1998) 2598–2602.
[86] T. Ma, K. Miyanishi, M.C.D. Trindade, M. Genovese, D. Regula, R.L. Smith, S. B. Goodman, Interleukin 1 receptor antagonist inhibits localized bone formation in vivo, J. Rheumatol. 30 (2003) 2547–2552.
[87] S.-H. Lee, T.-S. Kim, Y. Choi, J. Lorenzo, Osteoimmunology: cytokines and the skeletal system, BMB Rep. 41 (2008) 495–510.
[88] J. Lorenzo, The effects of immune cell products (cytokines and hematopoietic cell growth factors) on bone cells, in: Osteoimmunology Interact, Academic Press, Immune Skelet. Syst, 2015, pp. 143–167.
[89] K. Ishida, T. Matsumoto, K. Sasaki, Y. Mifune, K. Tei, S. Kubo, T. Matsushita, K. Takayama, T. Akisue, Y. Tabata, M. Kurosaka, R. Kuroda, Bone regeneration properties of granulocyte colony-stimulating factor via neovascularization and osteogenesis, Tissue Eng. - Part A. 16 (2010) 3271–3284.
[90] J. Street, M. Bao, L. DeGuzman, S. Bunting, F.V. Peale, N. Ferrara, H. Steinmetz, J. Hoeffel, J.L. Cleland, A. Daugherty, N. Van Bruggen, H.P. Redmond, R.A. D. Carano, E.H. Filvaroff, Vascular endothelial growth factor stimulates bone repair by promoting angiogenesis and bone turnover, Proc. Natl. Acad. Sci. U. S. A. 99 (2002) 9656–9661.
[91] M. Tang, L. Tian, G. Luo, X. Yu, Interferon-gamma-mediated osteoimmunology, Front. Immunol. 9 (2018).
[92] F.-C. Lin, H.A. Young, The talented interferon-gamma, Adv. Biosci. Biotechnol. 04 (2013) 6–13.
[93] H. Teng, H. Lin, Y. Huang, F. Lu, Formation of strontium-substituted hydroxyapatite coatings on bulk Ti and TiN-coated substrates by plasma electrolytic oxidation, Surf. Coat. Technol. (2018).